doi:10.20944/preprints202211.0118.v1

Article

Evidence for the Magnetoionic Nature of Oblique VHF Reflections from Midlatitude Sporadic-E Layers

Chris Deacon [1,*], Cathryn Mitchell [1], Robert Watson [1] and Ben Witvliet [2]

[1] Dept of Electronic and Electrical Engineering, University of Bath, Claverton Down, Bath, BA2 7AY, UK; cjd54@bath.ac.uk (C.D.); eescnm@bath.ac.uk (C.M.); eesrjw@bath.ac.uk (R.W.)
[2] Faculty of EEMCS, Radio Systems Group, University of Twente, 7500AE Enschede, The Netherlands; b.a.witvliet@utwente.nl
* Correspondence: cjd54@bath.ac.uk; Tel.: +44 7711 485324

Abstract: Mid-latitude sporadic-E (Es) is an intermittent phenomenon of the lower E region of the ionosphere. Es clouds are thin, transient, and patchy layers of intense ionization, with ionization densities which can be much higher than in the background ionosphere. Oblique reflection of radio signals in the very high frequency (VHF) range is regularly supported, but the mechanism for it has never been clearly established - specular reflection, scattering, and magnetoionic double refraction have all been suggested. This article proposes using the polarization behaviour of signals reflected from intense midlatitude sporadic-E clouds as an indicator of the true reflection mechanism. Results are presented from a measurement campaign in the summer of 2018, which gathered a large amount of data at a receiving station in the UK using 50 MHz amateur radio beacons as signal sources. In all cases the signals received were elliptically polarized, despite being transmitted with linear polarization; there were also indications that polarization behaviour varied systematically with the orientation of the path to the geomagnetic field. This represents, for all the examples recorded, clear evidence that signals were reflected from midlatitude Es by magnetoionic double refraction.

Keywords: sporadic-E; Es; ionosphere; mesosphere-lower thermosphere; VHF; polarization.

1. Introduction

Mid-latitude sporadic-E (commonly written as ‘Es’) is an intermittent phenomenon of the E region of the ionosphere, consisting of thin, transient, and patchy layers of intense ionization, with electron densities frequently much higher than those in the background ionosphere.

Because if its enhanced ionization density, sporadic-E can adversely affect a wide range of radio communications and radar systems, particularly those where the angle between the incident radio signal and the sporadic-E layer is very oblique [1]. Es can also cause scintillation on low-elevation satellite signals, including GNSS [2].

The mid-latitude form of sporadic-E [3 - 6], which is the focus of this study, consists of regions of high ionization at altitudes of 90-130 km [5, 7, 8] in thin layers up to a few km thick [9, 10] and with horizontal extent typically between a few km and a few hundred km [11]. The enhanced ionization density within Es clouds is caused by concentrations of long-lived metallic ions, ablated from meteors, and their associated free electrons [8, 10, 12]. Ions and neutrals are strongly coupled in the lower E region and there is a high degree of correlation between the occurrence of Es and the presence of sporadic metal layers [13 - 15].

Collisional coupling with neutrals causes the metal ions to be strongly affected by neutral winds. The wind shear theory [16, 17] is widely accepted as describing the principal mechanism behind mid-latitude Es-layer formation, by which vertical gradients in the zonal wind concentrate the metal ions into narrow height ranges [5, 18] through Lorentz forces. Observations that directly support this theory have recently come from a number of GNSS radio occultation and ionosonde studies [e.g., 19, 20]. For a more comprehensive overview of the characteristics of sporadic-E, see our earlier article [21, Section II] and references therein.

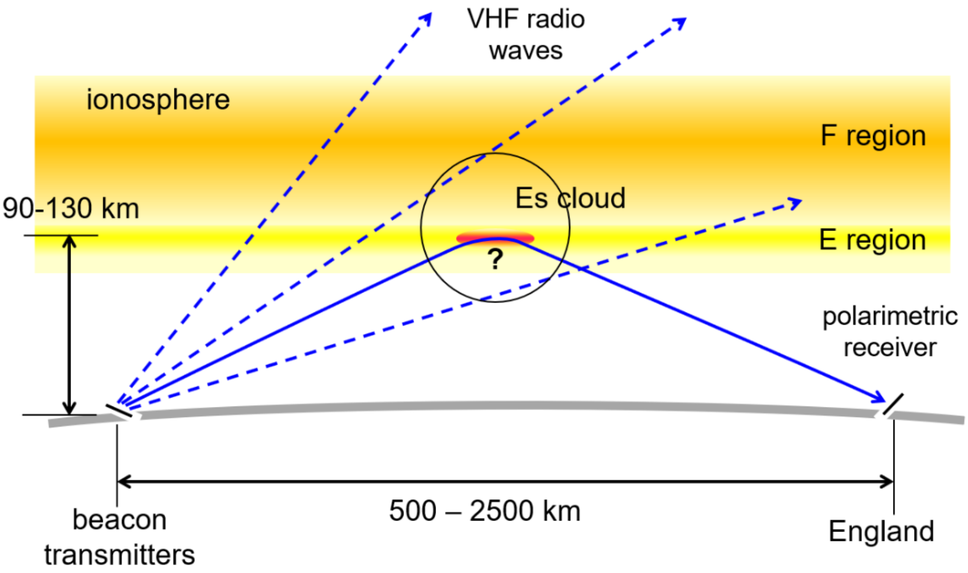

Figure 1. Reflection of VHF radio waves by sporadic-E (Es) clouds. Copyright IEEE [21].

Sporadic-E clouds regularly support oblique reflection of radio signals in the high frequency (HF) and very high frequency (VHF) ranges, up to at least 160 MHz [22] – see Figure 1. Although there is a clear consensus about the principal mechanisms of formation of sporadic-E, the process by which oblique VHF radio wave reflection from Es clouds occurs has never been clearly established. Authors have variously described it as specular reflection [23, 24], scattering [23, 25], or magnetoionic double refraction [26]. Each of these mechanisms will affect the polarization of the reflected signal differently, as discussed in Section 4.1.

The ionosphere consists of a partially ionized plasma in the presence of the Earth's magnetic field. It can be shown from the Appleton-Hartree equation [27, 28], which describes the relationship between the phase refractive index along the path of an electromagnetic wave and the local properties of the magnetized plasma, that only two wave modes, known as 'characteristic modes', can propagate. A linearly polarized wave entering the ionosphere must couple into a combination of the two characteristic modes.

The polarization of each of the characteristic modes can be represented by the quantity R, the complex ratio of two orthogonal linear components of the field strength [28, pp 8-20]:

$$R = -\frac{j}{Y_L}\left(\left[\frac{Y_T^2}{2(1-X-jZ)}\right] \mp \sqrt{\frac{Y_T^4}{4(1-X-jZ)^2}+Y_L^2}\right) \qquad (1)$$

where $X = \omega_N^2 / \omega^2$, $Y = \omega_B / \omega$, $Y_L = \omega_L / \omega$, $Y_T = \omega_T / \omega$, $Z = \nu / \omega$.

In (1), ω_N is the plasma frequency (the natural frequency of charge displacement), ω_B is the electron gyro frequency (the natural frequency at which electrons rotate around the magnetic lines of force), ω_L and ω_T are the longitudinal and transverse components of ω_B relative to the direction of propagation, and ν is the electron collision frequency. Y_L and Y_T are the magnetic terms and Z is the absorption term.

The two solutions of (1) correspond to the two characteristic modes, known as the 'ordinary' (O) and 'extraordinary' (X) waves, which are in general elliptically polarized and have opposite senses of rotation. Because the refractive index in the plasma for each of the modes is different and depends on local plasma and magnetic field conditions, the

doi:10.20944/preprints202211.0118.v1

O and X waves travel at different velocities and can follow significantly different paths. Note that the maximum usable frequency (MUF) on any given path is higher for the X mode than for the O mode, so that close to the MUF only the X mode may sometimes be reflected [29].

In the general case where both O and X modes are present on exiting the ionosphere, the resulting combined wave is elliptically polarized, with ellipticity and tilt angle depending on the amplitude, orientation, and phase relationship between the O and X waves at that point. The polarization of the wave reaching the receiver via magnetoionic double refraction can therefore be very different from that of the originally transmitted wave and can vary significantly as the relationship between the O and X waves changes.

Several experimental studies of the polarization of VHF signals after oblique Es reflection have been described in the literature [30, 31], although they give only limited information about the polarization state of the reflected wave. One study, however [32], reports more detailed observations of Es reflections from a single 55 MHz television transmitter over an 1160 km path. The results indicate that the received polarization was mainly elliptical, and that the major axis of the ellipse deviated significantly from the horizontal polarization of the transmitted signal.

Our own earlier work [21] describes a novel system for making radio wave polarization measurements of sporadic-E signals at 50 MHz, with higher temporal resolution and more accurately than has previously been possible. That article also presents an analysis of two case study recordings to prove the performance of the technique; for these two specific examples, received signals were clearly elliptically polarized rather than linearly polarized.

The current article reports the results of a polarization measurement campaign in the summer of 2018, which gathered a large amount of data at a receiving station in the south of the UK using six European amateur radio beacon transmitters, received via sporadic-E reflection, as 50 MHz signal sources. In Section 2, an overview of the measurement system is given, the scope of the measurement campaign is defined, and the data analysis approach is described. Section 3 describes the distribution of polarization parameters observed across all six beacons, plus a more detailed examination of the results for two similar propagation paths between which consistently differing signal polarization was observed. In Section 4, the results are discussed in the context of investigating the true nature of the reflection process, and outstanding issues are identified. Finally, in Section 5, conclusions are presented and opportunities for further work described.

2. Materials and Methods

2.1. Polarization measurement system

Our measurement system uses modern software-defined radio (SDR) techniques, which allow much higher cadence and more accurate measurement of the polarization parameters of received signals than has previously been possible. Care is taken to reduce environmental electromagnetic noise and to account for ground reflection effects. A summary of the approach is given here but we refer to our earlier article [21] for complete details, including equipment calibration, the minimization and compensation of environmental factors including ground reflection, and the estimated uncertainty in the measurements.

The measurement system consists of a pair of identical directional antennas, one oriented for horizontal polarization and the other for vertical polarization. The two antennas separately feed a dual channel, directly digitizing receiver, with its associated signal processing and data storage capability. See Figure 2.

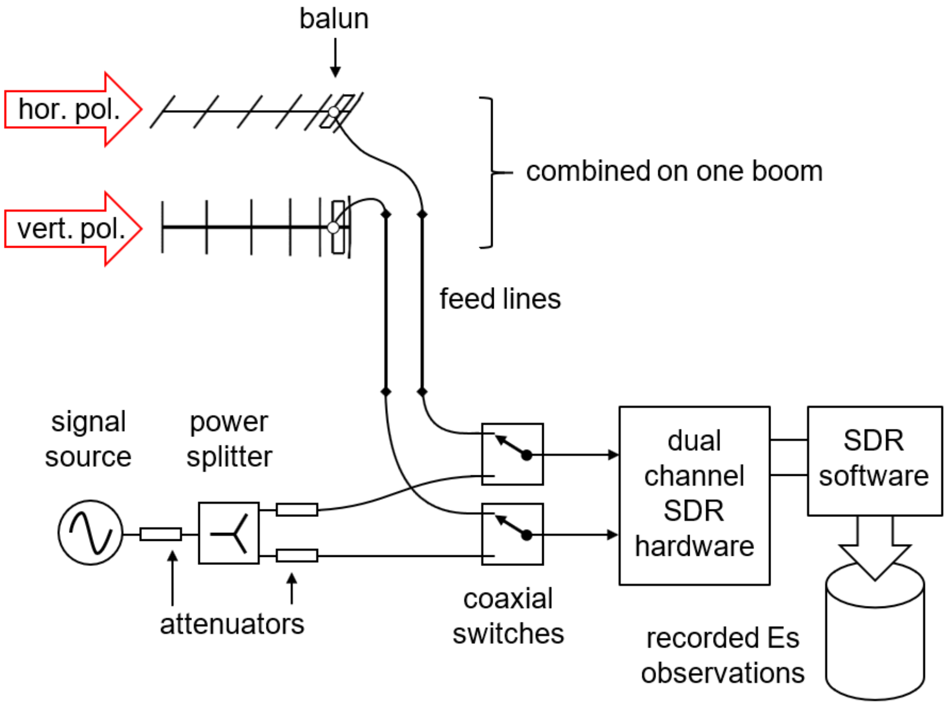

Figure 2. Measurement system block diagram. Copyright IEEE [21].

The two antennas are of a seven-element loop-fed (LFA) Yagi-Uda design and are interleaved orthogonally on the same boom. The LFA design was chosen because it has low gain for signals from the side and rear of the antenna; this is particularly important for the reduction of man-made electromagnetic noise, which typically dominates natural noise at 50 MHz at the receiving location. The antennas were mounted at a height of 20m above the ground in order to minimise environmental near-field effects, to further reduce the impact of local noise, and to maximize antenna gain at low elevation angles.

The dual receiver, an Apache Labs ANAN-8000DLE, digitally samples the two antenna inputs directly at the 50 MHz beacon frequency. The digital data stream is then filtered and down-sampled to produce four 16-bit data streams characterizing the in-phase and quadrature (IQ) components of the two sampled antenna voltages. These are then filtered further, to produce a narrow-band data stream (normally 6000 samples per second) which is stored on hard disk for post-processing. For calibration purposes, a stable comparison signal is manually switched to the two receivers at the beginning and/or end of each recording period.

In the post-processing stage, which is described in detail in [21], a single complex amplitude is calculated from each pair of I and Q samples. This data stream is then examined to identify the useful time segment(s) of the recording, to determine the precise frequencies of the beacon and calibration signals, and to identify a clear frequency for ambient noise level measurement. This information is used to extract beacon, calibration, and noise data streams for the desired time segment, each filtered to a 25 Hz bandwidth.

The calibration signal is used to derive correction factors to compensate for receiver offsets and drift, including differential amplitude, differential phase, and absolute power. These correction factors are then applied to the filtered beacon data streams, along with static corrections for differential antenna cable loss and phase lag. The effect of the ground reflection in front of the antenna is also compensated for.

The beacon data streams are then cleaned by removing samples which are less than 10 dB above the average ambient noise level on each channel and by using a ‘dynamic squelch’ to remove as much as possible of the beacon’s periodic morse code identification message.

Finally, per-sample polarization parameters are calculated from the filtered, calibrated, and cleaned data. The power ratio and the phase difference between the vertically and horizontally polarized signals are directly measured; from them, the full polarization characteristics of the wave can be calculated.

2.2. Signal sources

Six European amateur radio 50 MHz beacon transmitters were used as signal sources. These beacons operate at frequencies between 50.4 MHz and 50.5 MHz, continuously transmitting narrow-band signals on a 24-hour basis. Power output is low, typically 1 – 10 W, and antennas are normally omnidirectional and linearly polarized. The beacons transmit a continuous carrier plus a periodic station identification in Morse code.

The great circle paths from the beacons to our measurement location at Churt in the south of England (51.135 N, 0.784 W) were over distances between 1,100 km and 1,650 km, and over a range of orientations to the Earth's magnetic field – see Figure 3. The minimum great circle distance was selected to reduce the possibility that other propagation modes (such as tropospheric ducting) were present. The maximum distance was chosen to reduce the likelihood of double-hop Es propagation with an intermediate ground reflection, so that the likely reflection zone, close to the path midpoint, can more easily be identified. Note that in western Europe, magnetic North is within a few degrees of geographical North.

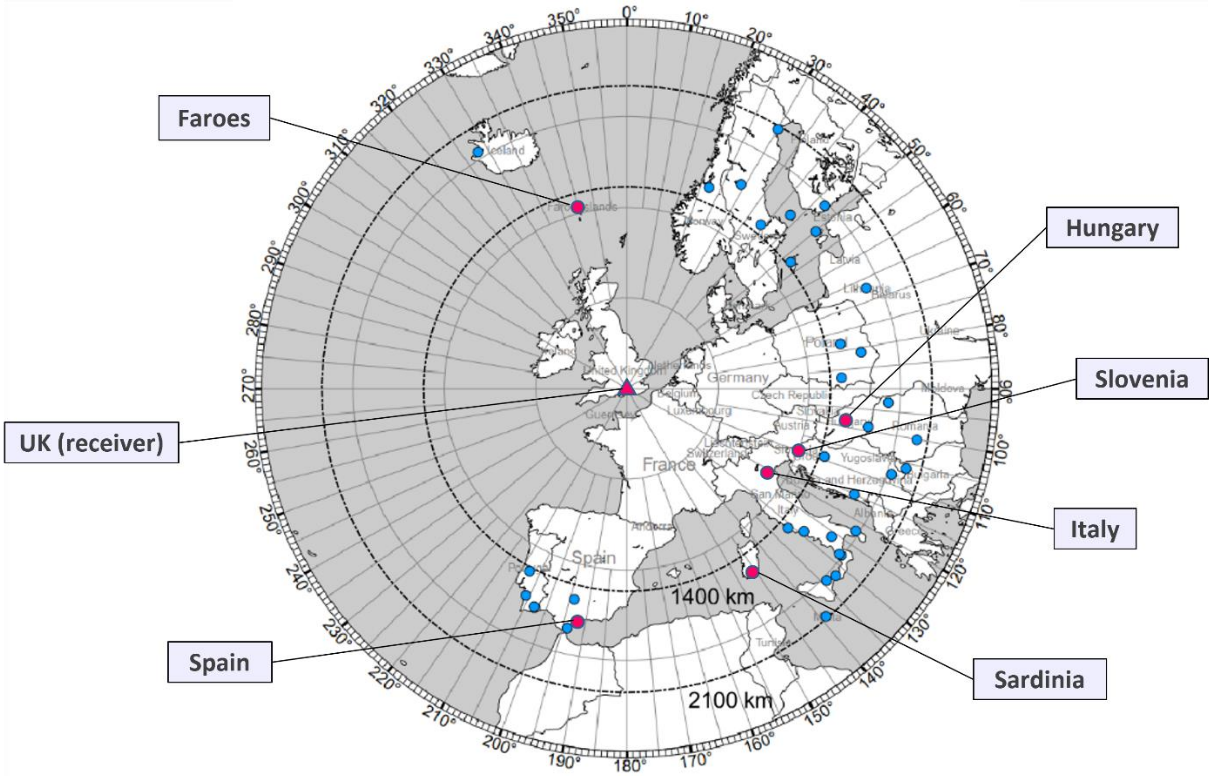

Figure 3. Azimuthal map centered on the receiving station, showing the locations of amateur 50 MHz beacon transmitters at distances between 1000 km and 2100 km. The red triangle marks the receiving station; red dots indicate the beacons included in the polarization measurement campaign; blue dots indicate other beacons. Background map courtesy Tom Epperly. Adapted from [21], which is copyright IEEE.

Table 1 lists the parameters of the beacons observed for this study, showing for each beacon its location, the great circle distance from the receiver, its transmission frequency, and its antenna polarization. The number of separate dates on which the beacon was observed, and the total duration of fully calibrated data, are also shown.

doi:10.20944/preprints202211.0118.v1

Table 1. Amateur radio beacons observed during the 2018 measurement campaign

Location	Identifier	Latitude [deg]	Longitude [deg]	Great circle distance [km]	Frequency [MHz]	Transmit antenna polarization*	Dates observed	Total duration [mins]
Faroe Islands	OY6BEC	62.063	- 6.958	1,270	50.402	Horizontal	1	40.0
Spain	ED7YAD	36.604	- 4.625	1,644	50.475	Horizontal	2	6.0
Sardinia	IQ0AM	39.229	9.208	1,536	50.448	Vertical	1	8.4
Italy	IZ3QWJ	45.104	11.625	1,138	50.477	Vertical	1	18.8
Slovenia	S55ZRS	46.104	15.042	1,288	50.422	Vertical	4	23.5
Hungary	HG7BVA	47.396	19.375	1,516	50.430	Vertical	6	109.2

* Note that the true polarization of the signal transmitted towards the receiver may not be exactly horizontal or vertical, because of the near-field influence of masts, enclosures, or other antennas.

2.3. Characterization of polarization state

Linear and circular polarization are both special cases of the general form - elliptical polarization. As shown in Figure 4, the shape and orientation of the polarization ellipse can be characterized by its axial ratio, defined as the ratio of the major axis to the minor axis, and its tilt angle, measured clockwise to the major axis from the horizontal. A pure circularly polarized wave has an axial ratio of 1, and a pure linearly polarized wave has an axial ratio of infinity. All other values of axial ratio correspond to elliptical polarization.

Note that the IEEE standard definitions [33, 34] of these parameters are adopted in this article, according to which both the sense of rotation of the ellipse and the tilt angle are defined looking along the direction of travel of the wave away from the transmitter. The axial ratio is defined to be positive when the sense of rotation is right-handed, and negative when the sense of rotation is left-handed.

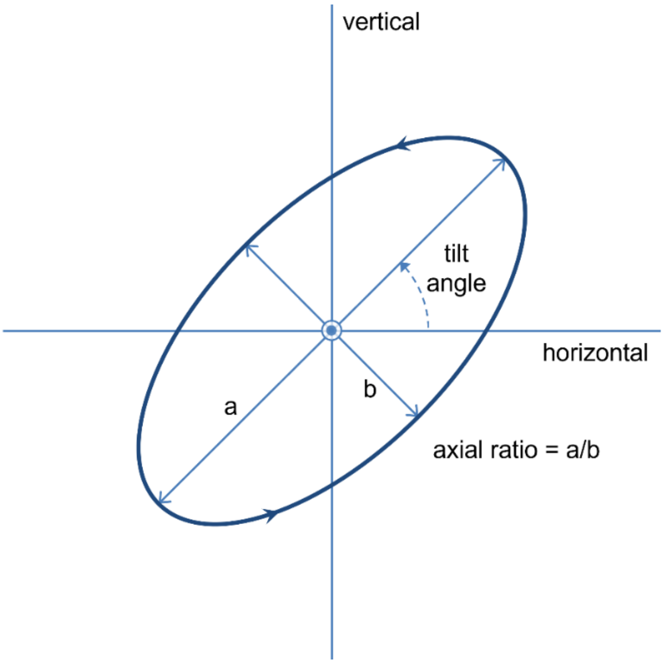

Figure 4. The key parameters of the polarization ellipse of an incoming wave, illustrating the definitions of axial ratio and tilt angle. The wave direction is out of the page towards the viewer. The arrows on the ellipse show a right-handed sense of rotation. The IEEE standard definitions of sense of rotation and tilt angle have been adopted; both are defined looking along the direction of travel of the wave away from the transmitter.

Following the IEEE conventions, it can be shown [34, 35] that, for the axial ratio *ar* and tilt angle τ of the polarization ellipse [21]:

$$ar = -cot\left(sin^{-1}\left(\frac{2P\,sin\,\varphi}{[1+P^2]}\right)/2\right) \tag{2}$$

$$\tau = tan^{-1}\left(\frac{2P\,cos\,\varphi}{[1-P^2]}\right)/2 \tag{3}$$

$$If\ P > 0,\ \tau = \tau - sgn(\tau)\frac{\pi}{2} \tag{3a}$$

where P is the ratio of the vertical field strength to the horizontal field strength and φ is the phase difference between the two fields. Tilt angle τ is defined to be in the range ± 90°.

Using the polarization measurement system described in Section 2.1, and for a polarization state typical of observations reported in this article, the per-sample expanded standard uncertainty (95% confidence) in axial ratio is estimated to be 1.3, and in tilt angle 4.3° [21].

For some purposes, a more useful way to represent the polarization state of an electromagnetic wave is the Poincaré Sphere [35, 36, 37, 38], in which key polarization characteristics are plotted on the surface of a unit sphere using a normalized, three-dimensional, spherical coordinate system. Each possible polarization state maps uniquely to a point on the surface of the sphere – see Figure 5.

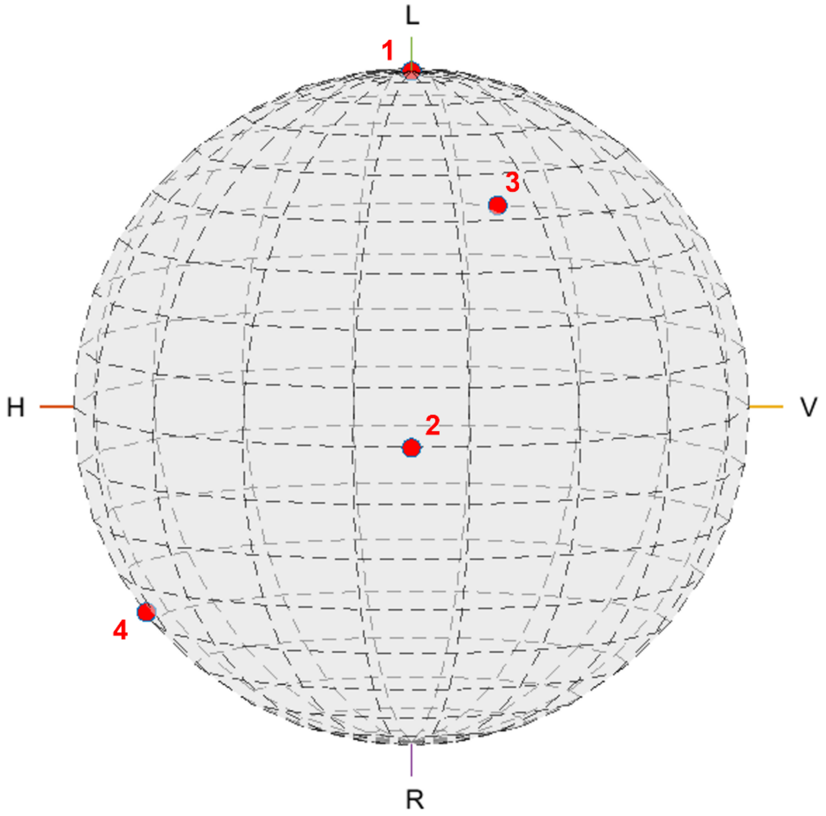

Figure 5. Illustrating the Poincaré Sphere. Pure left-hand circular polarization is at the 'North Pole' and pure right-hand circular polarization is at the 'South Pole'. Linear polarization is plotted at the 'Equator', with (in this orientation) pure horizontal (τ = 0°) to the left and pure vertical (τ = ± 90°) to the right. Note that, in this view, negative tilt angles would appear on the rear surface of the sphere. Example polarization state mappings are marked with red dots (1: LH circular; 2: Linear, tilt angle + 45°; 3: LH elliptical, tilt angle + 55°/axial ratio - 2.5; 4: RH elliptical, tilt angle + 7°/axial ratio + 3).

doi:10.20944/preprints202211.0118.v1

On the surface of the sphere, the ‘longitude’ is twice the tilt angle τ as defined in (3), and the ‘latitude’ is twice the ellipticity angle ε, which is related to the axial ratio by [36]:

$$\varepsilon = \cot^{-1}(-ar) \tag{4}$$

It follows that the ‘North Pole’ of the Poincaré Sphere maps to pure left-hand circular polarization and the ‘South Pole’ maps to pure right-hand circular polarization. The ‘Equator’ maps to linear polarization, with pure horizontal at 0° ‘longitude’, pure vertical at 180° ‘longitude’, and other linear orientations around the equator line. Away from the ‘Equator’ and the poles, polarization states in the ‘Northern Hemisphere’ are left-hand elliptically polarized, and in the ‘Southern Hemisphere’, right-hand elliptically polarized.

The Poincaré Sphere gives a straightforward visual representation of the polarization state and has several useful features. Particularly relevant to this study is that a sequence of states can be plotted on the surface of the sphere, to reveal how the polarization of a signal changes over time. In addition, the Poincaré Sphere can clearly reveal complete or partial depolarization. While a fully polarized wave will always appear to be on the surface of the sphere, a partially polarized wave will appear to be inside the sphere and a completely unpolarized wave will be at the center [39].

3. Results

Sporadic-E is an intermittent phenomenon which is very localized and difficult to predict, meaning that an opportunistic approach must be taken if a useful amount of data is to be gathered. There is a strong maximum in the incidence of Es in the hemispheric summer [30, 40, 41], so the period from May to August was chosen for the measurement campaign in 2018. The polarization measurement system described in Section 2.1 was used to gather a large amount of data at a receiving station in the south of the UK, using six European amateur radio beacon transmitters as sources, as described in Section 2.2.

The measurement campaign was in two parts. In the first part, a general survey was conducted, focused on gathering data from as many sources as possible over great circle paths at a range of distances, and orientations to the Earth’s magnetic field. The aim of this work was to establish the general nature of the received polarization, and specifically whether it was normally elliptical or linear, in order to throw light on the nature of reflection from sporadic-E. The results of this part of the study are described in Section 3.1.

The second part of the study focused on a more in-depth study of the signals from Slovenia and Hungary. These two great circle paths are close to each other, and each is roughly perpendicular to the Earth’s magnetic field at the estimated point of reflection. Repeated measurements were made over multiple days. The results of this phase are reported in Section 3.2.

3.1. General survey results

The survey element of the campaign gathered data from all six signal sources shown in Table 1 (Section 2.2), with a total of 206 minutes of clean data gathered across 14 separate Es events. The volume of data is not uniform across sources because of the sporadic nature of Es, but there is enough to clearly identify polarization behaviour in each case.

In order to establish an overall picture of polarization behaviour, Figures 6 – 11 show the distribution of axial ratio and tilt angle measurements for each beacon in histogram form. In each Figure, histogram (a) shows measured axial ratio on the horizontal axis on a logarithmic scale, with circular polarization marked by the red line in the center. Left-hand elliptical polarization is to the left of the red line and right-hand elliptical polarization is to the right of the red line. Similarly, histogram (b) shows measured tilt angle, with the red line marking 0° (horizontal) and with negative angles to the left, positive angles to the right. In each case, the vertical axis is the proportion of the measurements per bin.

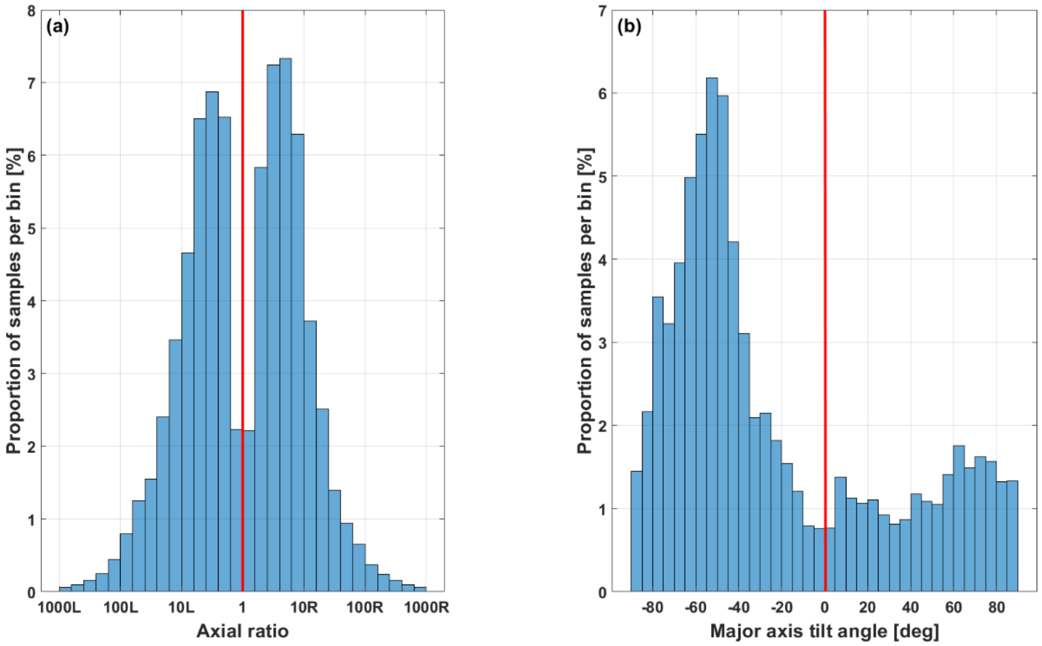

Figure 6. Faroe Islands: 8 August 2018, total 40 mins at 6,000 samples s^{-1}.
(a) Axial ratio histogram. Horizontal axis: axial ratio (logarithmic scale). Red center line: axial ratio = 1 (circular polarization). Left of center line: left-hand elliptical polarization. Right of center line: right-hand elliptical polarization. Vertical axis: proportion of samples per bin.
(b) Tilt angle histogram. Horizontal axis: tilt angle (linear scale). Red center line: tilt angle = 0° (horizontal). Left of center line: negative tilt angle. Right of center line: positive tilt angle. Vertical axis: proportion of samples per bin.

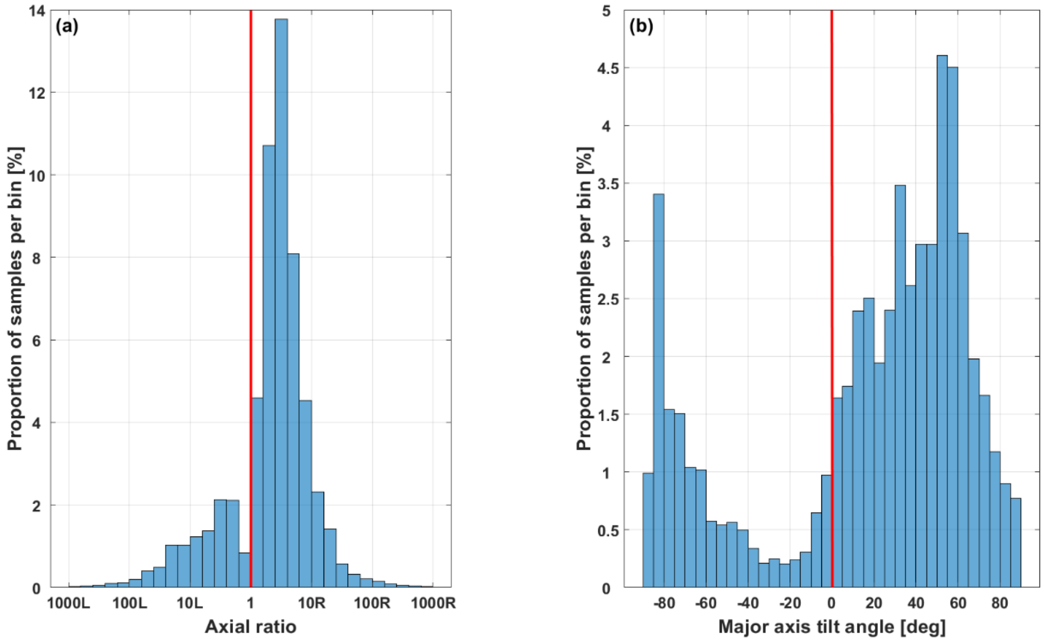

Figure 7. Spain: 29 July, 6 August 2018, total 6 mins at 6,000 samples s^{-1}.
(a) Axial ratio histogram. Horizontal axis: axial ratio (logarithmic scale). Red center line: axial ratio = 1 (circular polarization). Left of center line: left-hand elliptical polarization. Right of center line: right-hand elliptical polarization. Vertical axis: proportion of samples per bin.
(b) Tilt angle histogram. Horizontal axis: tilt angle (linear scale). Red center line: tilt angle = 0° (horizontal). Left of center line: negative tilt angle. Right of center line: positive tilt angle. Vertical axis: proportion of samples per bin.

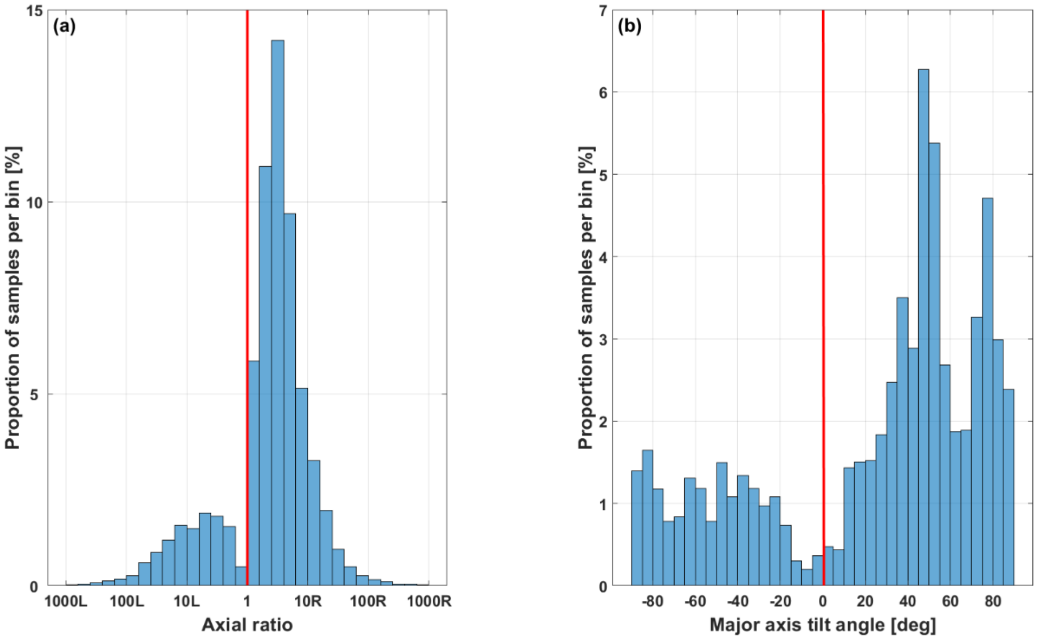

Figure 8. Sardinia: 8 August 2018, total 8.4 mins at 6,000 samples s^{-1}.
(a) Axial ratio histogram. Horizontal axis: axial ratio (logarithmic scale). Red center line: axial ratio = 1 (circular polarization). Left of center line: left-hand elliptical polarization. Right of center line: right-hand elliptical polarization. Vertical axis: proportion of samples per bin.
(b) Tilt angle histogram. Horizontal axis: tilt angle (linear scale). Red center line: tilt angle = 0° (horizontal). Left of center line: negative tilt angle. Right of center line: positive tilt angle. Vertical axis: proportion of samples per bin.

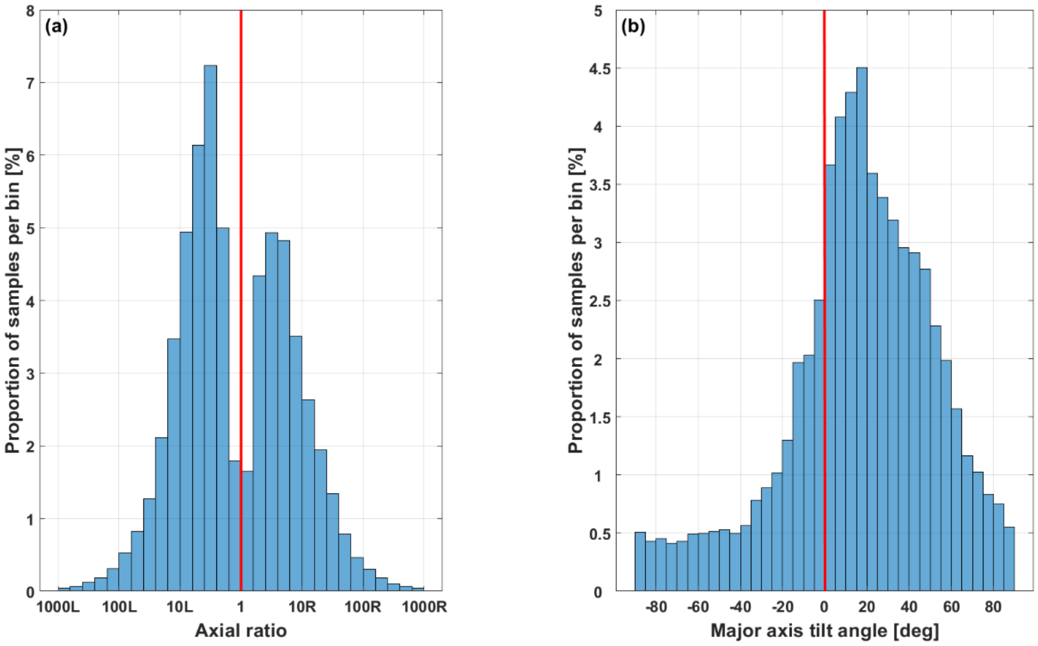

Figure 9. Italy: 2 August 2018, total 18.8 mins at 6,000 samples s^{-1}.
(a) Axial ratio histogram. Horizontal axis: axial ratio (logarithmic scale). Red center line: axial ratio = 1 (circular polarization). Left of center line: left-hand elliptical polarization. Right of center line: right-hand elliptical polarization. Vertical axis: proportion of samples per bin.
(b) Tilt angle histogram. Horizontal axis: tilt angle (linear scale). Red center line: tilt angle = 0° (horizontal). Left of center line: negative tilt angle. Right of center line: positive tilt angle. Vertical axis: proportion of samples per bin.

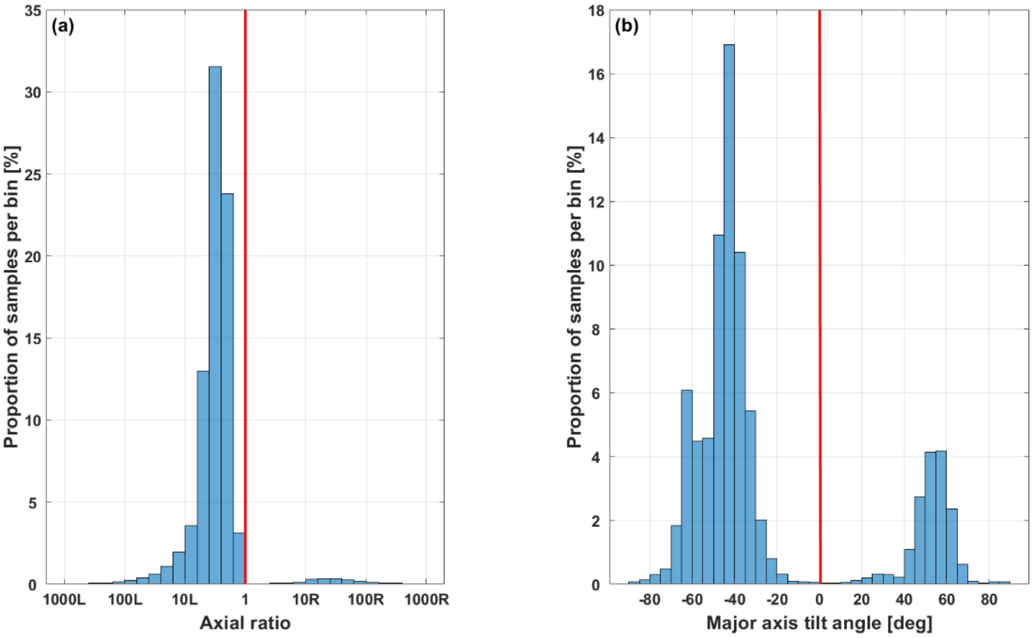

Figure 10. Slovenia: 29 July, 15, 18, 20 August 2018, total 23.5 mins at 6,000 samples s^{-1}.
(a) Axial ratio histogram. Horizontal axis: axial ratio (logarithmic scale). Red center line: axial ratio = 1 (circular polarization). Left of center line: left-hand elliptical polarization. Right of center line: right-hand elliptical polarization. Vertical axis: proportion of samples per bin.
(b) Tilt angle histogram. Horizontal axis: tilt angle (linear scale). Red center line: tilt angle = 0° (horizontal). Left of center line: negative tilt angle. Right of center line: positive tilt angle. Vertical axis: proportion of samples per bin.

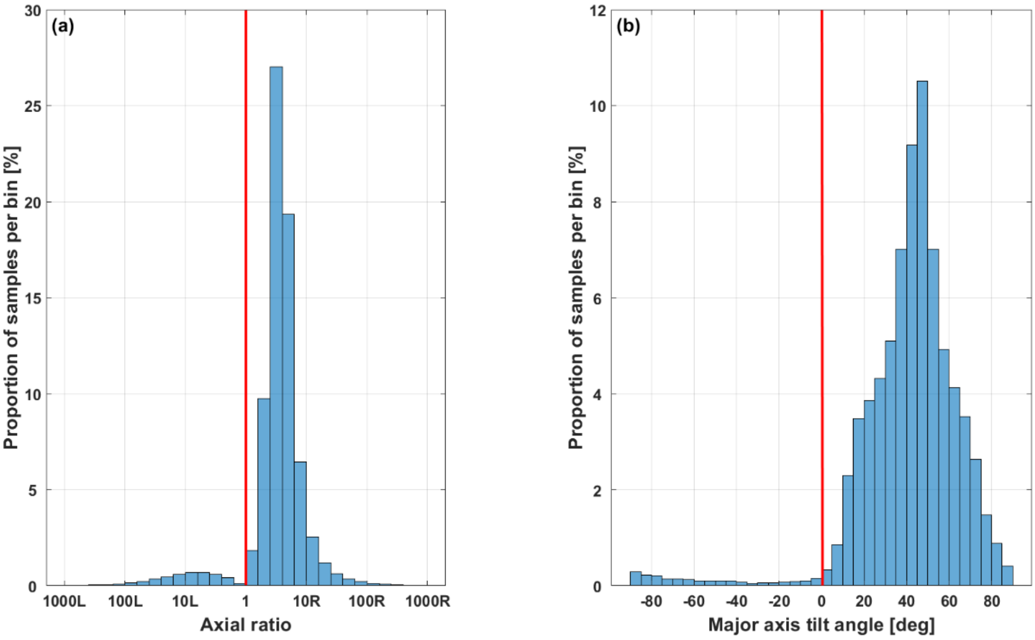

Figure 11. Hungary: 26 June, 23, 29 July, 1, 18, 20 August 2018, total 109.2 mins at 6,000 samples s^{-1}.
(a) Axial ratio histogram. Horizontal axis: axial ratio (logarithmic scale). Red center line: axial ratio = 1 (circular polarization). Left of center line: left-hand elliptical polarization. Right of center line: right-hand elliptical polarization. Vertical axis: proportion of samples per bin.
(b) Tilt angle histogram. Horizontal axis: tilt angle (linear scale). Red center line: tilt angle = 0° (horizontal). Left of center line: negative tilt angle. Right of center line: positive tilt angle. Vertical axis: proportion of samples per bin.

For the Faroe Islands beacon (Figure 6), it can be seen that the polarization of the signal varied over a wide range during the 40 minutes analyzed, which was made up of regular extracts from a single sporadic-E event which was over 90 minutes long. In this analysis there is no clearly preferred sense of rotation, with right-hand and left-hand elliptical polarization occurring roughly equally. In each case, the median magnitude of the axial ratio was about 3, and although tilt angle varied widely, there was a clear preference for angles around – 45°.

In the case of Spain (Figure 7), both senses of rotation were again observed, but with a clear preference for right-hand elliptical polarization and a median axial ratio of just under + 3. The tilt angle for the polarization ellipse varied widely, with a primary peak at about + 45° and a secondary peak at about - 80°.

The results from Sardinia (Figure 8) are similar to those from Spain, again with a clear preference for right-hand elliptical polarization and with a median axial ratio of just under + 3. The variation in tilt angle was also similar to Spain, but in this case the primary peak was around + 55°.

The distribution of polarization states of the signal from Italy (Figure 9) is much more similar to that observed from the Faroe Islands, with a near-symmetrical axial ratio distribution. The sense of rotation reversed many times during the recording, although in this case there was a slight preference for left-hand elliptical polarization over right-hand. The median of the left-hand elliptical measurements is at an axial ratio of about + 4. Tilt angles again varied widely, albeit with a broad peak in the distribution centered at about + 30°.

Finally, the polarization histograms for the beacons in Slovenia (Figure 10), and Hungary (Figure 11) look quite different from the other beacons. Each shows a very well-defined sense of rotation and a narrow peak in axial ratio. But the Slovenian signals exhibit distinct left-hand elliptical polarization, with a median axial ratio of – 3.1, whereas the Hungarian signals exhibit very clear right-hand elliptical polarization with a median axial ratio of + 3.6. Tilt angles also show a comparatively narrow range of variation, with Slovenia exhibiting a strong peak around - 45° and Hungary showing a strong peak in the opposite quadrant, at about + 50°, see Section 3.2.

It can be seen from Figures 6 to 11 that, across all the data, polarization states approaching linear - that is, with large axial ratio values - are comparatively rare. Signals from all the beacons, for the overwhelming majority of the time, are clearly elliptically polarized.

3.2. Case study – Slovenia and Hungary beacons

The second part of the study was a more detailed review of the data for the Slovenia and Hungary beacons, beyond the summaries in Figures 10 and 11. As has been seen, analysis for each beacon shows strongly defined elliptical polarization, but the sense of rotation and predominant tilt angle behaviours are consistently opposite from each other.

Firstly, we will consider a pair of individual recordings made only ten minutes apart on 18 August 2018, during a long sporadic-E event over western Europe. The development and movement of this particular event is described in one of our earlier articles, using crowdsourced amateur radio reception reports as indicators of the presence of intense sporadic-E [42].

Figure 12 shows amateur radio signal reports from across Europe for the 15-minute period which includes the ‘case study’ polarization measurements. Superimposed on the map are the locations of the beacons and the great circle paths from the beacons to the receiving site in the UK. The great circle midpoints are marked, as approximate indications of the sporadic-E reflection points. It can be seen from the map that the two great circle midpoints are over southern Germany, about 200 km apart, and that there is strong evidence for the presence of intense sporadic-E in that area and at that time. Note also that magnetic north is within 2° of geographical north in this part of Europe [43].

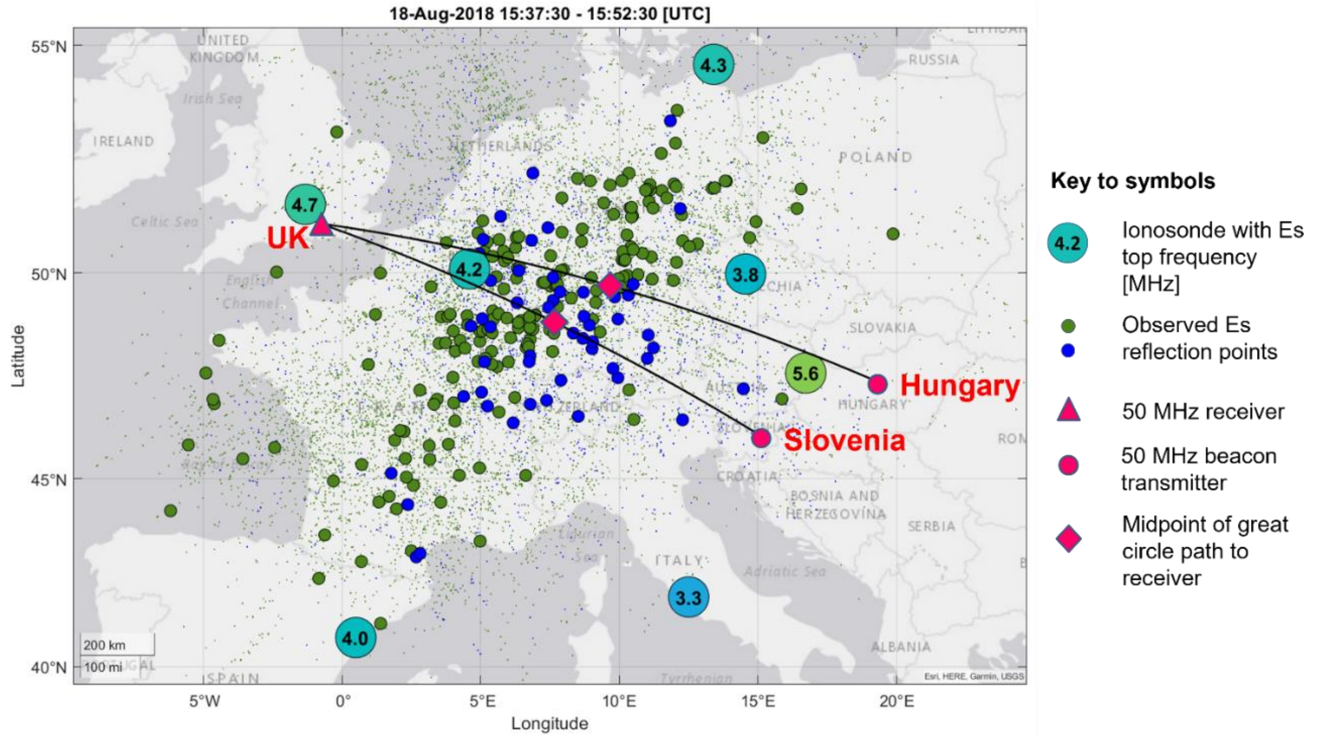

Figure 12. European sporadic-E event 18 August 2022 15:37:30 – 15:52:30 UTC, mapped using amateur radio signal reports. Slovenia and Hungary beacons and UK receiving location marked. Black lines: great circle paths from beacons to receiver with midpoints indicated. Adapted from [42].

To illustrate the consistent difference in polarization for signals over these adjacent paths, Supplementary Video 1 shows a one-minute quasi-real time replay of the measured, normalized, polarization ellipse for the Slovenia beacon on 18 August 2018, and Video 2 likewise for the Hungary beacon, recorded less than ten minutes later. Figure 13 shows a snapshot from each video.

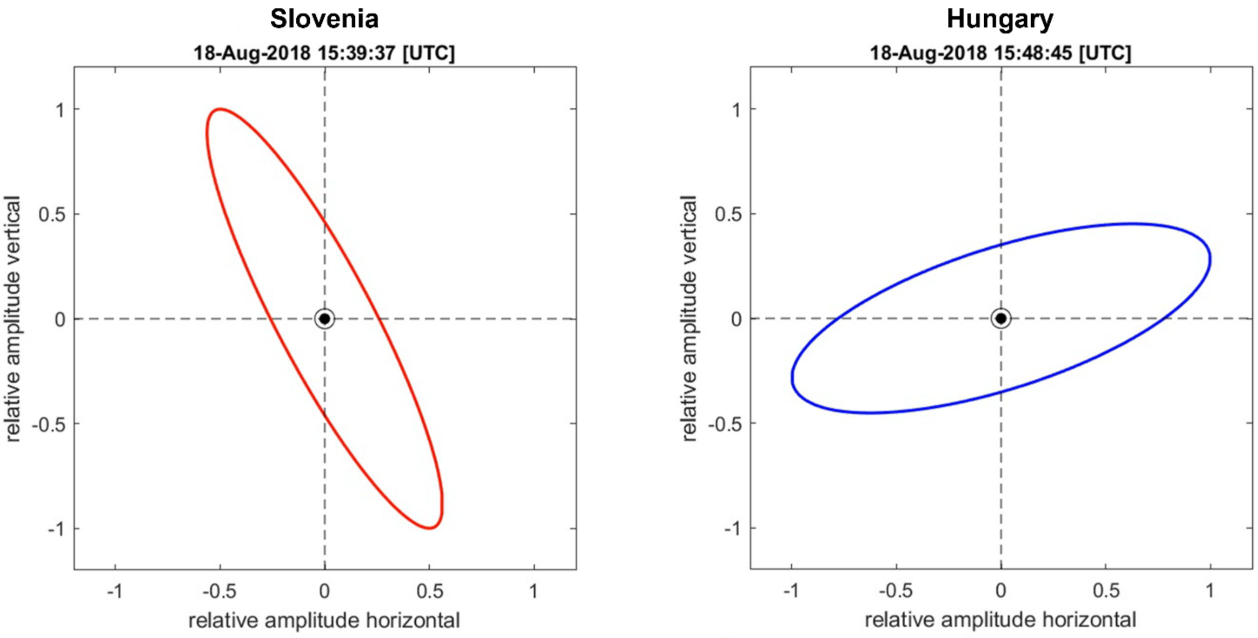

Figure 13. Illustrative snapshots from Supplementary Video 1 (left) and Supplementary Video 2 (right), showing the measured normalized polarization ellipse for the Slovenia and Hungary beacons respectively. Blue = right-hand sense of rotation, red = left-hand sense of rotation.

By contrast, referring back to Figure 6, the signals from the Faroe Islands on 8 August 2018 show polarization varying over a wide range of axial ratio and tilt angle states. This behaviour was repeated at shorter timescales as well, as is very clearly illustrated in Supplementary Video 3. This video shows two-minute quasi-real time replay of the measured, normalized, polarization ellipse for the Faroes beacon on 8 August 2018. It can be seen that the axial ratio, tilt angle, and sense of rotation are all constantly changing, on a timescale of seconds.

Using a Poincaré sphere to show how the measured polarization of a typical signal varies, Figure 14 shows the 18 August 2018 case study data for the Hungarian beacon (two minutes duration) plotted as described in Section 2.3.

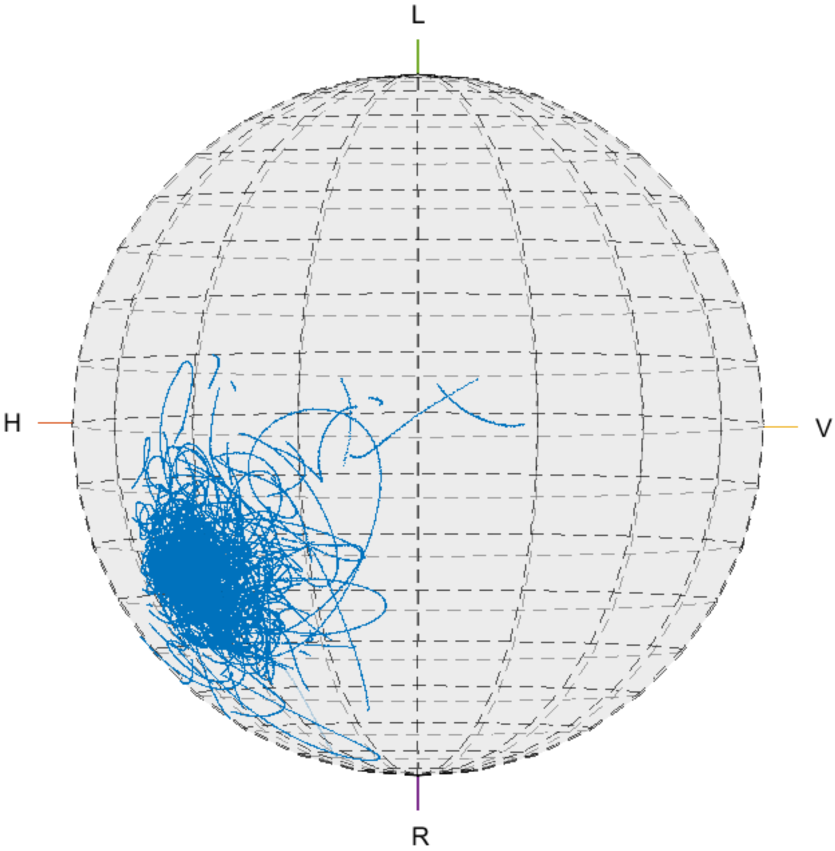

Figure 14. Poincaré sphere representation of the measured polarization state for the Hungary beacon, 18 August 2018 15:48:26 – 15:50:26 UTC, recorded at 6,000 samples s^{-1}. View slightly rotated to show detail: center line = major axis tilt angle of + 40°.

From Figure 14, a number of observations can be made. Firstly, all of the data is plotted onto the surface of the sphere rather than inside it. This indicates that the signal is consistently fully polarized. Secondly, there is a clear 'home' state for the polarization, in this case in the lower left front quadrant of the sphere, corresponding to right-hand elliptical polarization with a tilt angle between 0° and + 45°. Deviations from the home state are present but there is a tendency to revert towards the home state. Thirdly, the deviations away from the home state can be seen to take smooth paths on the surface of the sphere rather than jagged, irregular paths, indicating a relatively smooth evolution of polarization. Gaps in the tracks indicate that some measurements have been rejected in post-processing because of low signal to noise ratio (see Section 2.1).

Figure 15 (Slovenia) and Figure 16 (Hungary) each show a set of representative Poincaré spheres to illustrate the general pattern of polarization behaviour over a number of days, with one sample sphere for each day that the beacon in question was observed.

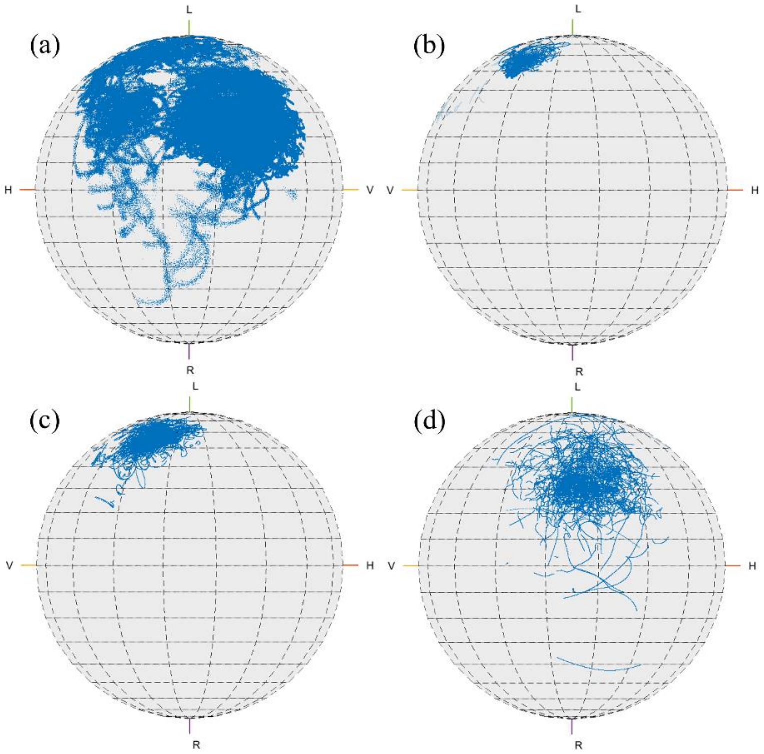

Figure 15. Slovenia beacon: Poincaré sphere representation of measured polarization state for representative samples from each of four days: (a) 29 July; (b) 15 August; (c) 18 August; (d) 20 August 2018. Sample rate (a): 24,000 samples s^{-1}; (b) – (d): 6,000 samples s^{-1}. Spheres (b) – (d) rotated to show the 'rear' of the sphere (negative tilt angles).

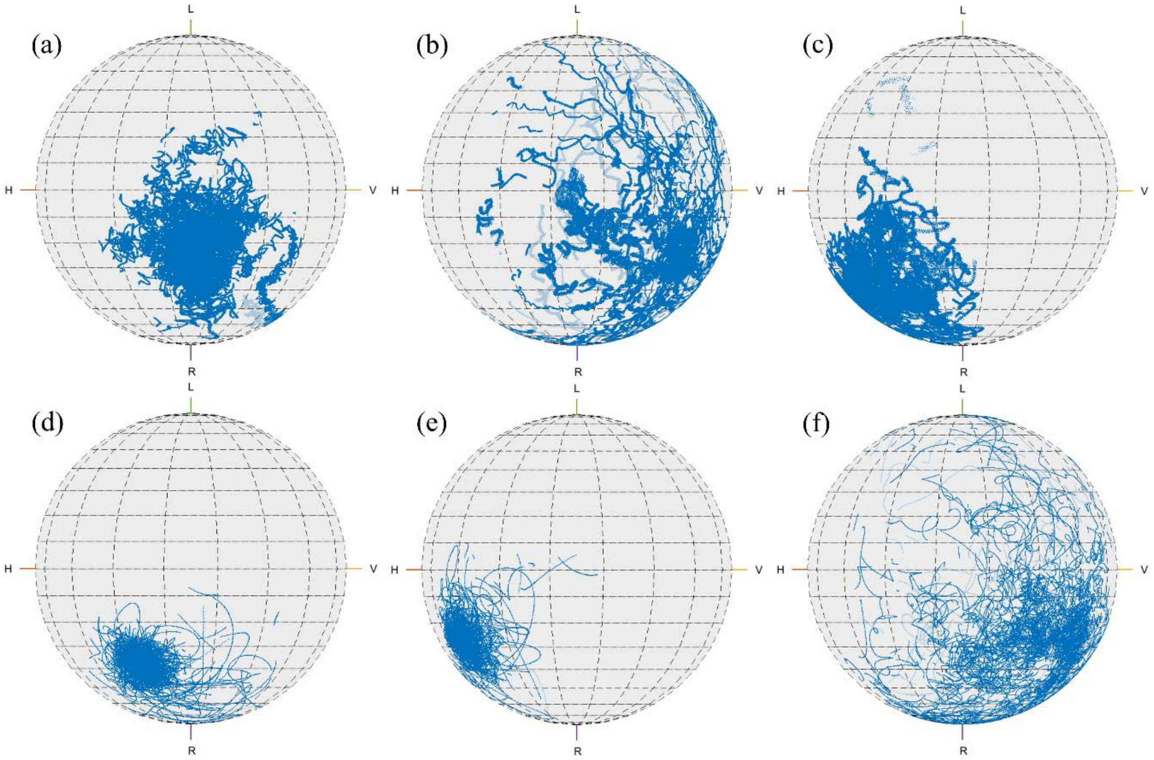

Figure 16. Hungary beacon: Poincaré sphere representation of measured polarization state for representative samples from each of six days: (a) 26 June; (b) 23 July; (c) 29 July; (d) 1 August; (e) 18 August; (f) 20 August 2018. Sample rate (a) – (c): 24,000 samples s^{-1}; (d) – (f): 6,000 samples s^{-1}.

doi:10.20944/preprints202211.0118.v1

It can be seen from Figures 15 and 16 that the polarization states are broadly consistent across the full set of measurements of signals from Slovenia and Hungary. Both beacons show full polarization, with no indication of depolarization. It can be seen that there is, in each case, a relatively localized home state, although the range of deviations from it varies. The home state appears at various axial ratios and (particularly) a range of tilt angles on different days, but nonetheless the preferred sense of rotation is consistent for each beacon.

The tilt angle for the Hungary beacon is variable but is consistently between 0° and + 90°, corresponding to the top right-hand quadrant of Figure 4. The one outlier from a consistent pattern is for the Slovenia beacon, for which, although three of the spheres show negative tilt angles corresponding to the top left-hand quadrant of Figure 4, one sphere - Figure 15 (a) - indicates tilt angles corresponding to the top right-hand quadrant of Figure 4.

4. Discussion

4.1. Mode of reflection

The clear result of the measurement campaign (Section 3) is that, in every case, the signals received were elliptically polarized after reflection from the Es cloud. This is despite the fact that all the beacons were known to be transmitting with linear polarization. Received signals exhibited no evidence of depolarization, and there are indications that polarization behaviour varied systematically depending on the orientation of the path to the geomagnetic field at the point of reflection. This is convincing evidence that radio wave reflection from intense midlatitude sporadic-E layers at 50 MHz is mainly by magnetoionic double refraction, rather than by either scattering or specular reflection.

The term ‘scatter’ has been used in the literature to describe a mechanism for producing weak sporadic-E signals, with differentiation being made between scatter and ‘true’ reflection on the basis of measured transmission loss [23, 25]. According to this model, Es scattering is caused by irregularities in electron density, within an Es cloud, which are significantly larger than the wavelength of the incident wave but significantly smaller than the extent of the wavefront.

Ionospheric scattering of VHF radio waves [44 pp 470 – 476] is caused by small-scale irregularities in electron density, the effect of which is to scatter energy away from the wave direction. At small angles to the wavefront, which are the most relevant to the current discussion (‘forward scatter’), the polarization of the incident wave is largely preserved [45]. At larger scatter angles, increasing amounts of depolarization occur because of the random location, movement, and orientation of the scattering centers. Overall, scatter effects cannot change a linearly polarized wave into an elliptically polarized wave. Scatter from inhomogeneities within the sporadic-E layer may well cause the propagation of weak signals under some conditions, but it will not explain the properties of the stronger signals propagated via intense sporadic-E as observed in this study.

Turning now to the possibility of ‘specular reflection’, it is obvious that the term in its normal sense, referring to mirror-like reflection at a hard surface, cannot apply physically. The ionosphere is a partially ionized plasma; it does not consist of a closely-spaced matrix of atoms, such as in a metal or a solid dielectric, but rather is made up of randomly and widely-spaced ions and electrons which are in constant motion within the neutral atmosphere. The question is, therefore, whether signals returned from sporadic-E layers have similar characteristics to waves reflected from a hard surface, not whether they are actually being reflected from such a surface.

In the ionosphere, the refractive index is always less than 1 and it decreases as ionization density increases [44], so total internal reflection must be considered the most appropriate model. It can be shown [46, pp 96-101] that total internal reflection of an electromagnetic wave at a dielectric surface introduces a fixed phase difference between the two components of the reflected wave parallel to and perpendicular to the surface. However, at the grazing angles of incidence relevant to long-distance reflection of 50 MHz waves from sporadic-E clouds, such a phase difference will be very small (< 3°) [47, pp 49–50], and dependent only on the alignment of the wave direction with the reflecting surface.

Although the internally reflected wave would therefore be slightly elliptically polarized rather than purely linear, reflection from such a 'mirror' could neither produce the large values of axial ratio and tilt angle reported in Section 3, nor the observed variation of polarization behaviour with the orientation of the path to the geomagnetic field.

4.2. Detailed polarization behaviour

All the observed polarization features are consistent with magnetoionic double refraction within a variable-density sporadic-E layer, but a complete model would need to be able to explain more detailed polarization behaviour as well.

It can be seen from Section 3.1 that, in most orientations to the magnetic field, all the key properties of the polarization ellipse – sense of rotation, axial ratio, and tilt angle - are highly variable. However as described in Section 3.2, in the special case of the two paths which are closest to perpendicular to the geomagnetic field at the reflection point, much more stable elliptical polarization was observed over multiple sporadic-E events, with consistently opposite polarization properties for the two paths.

As wave frequency increases, the two characteristic waves more closely approach circular polarization [44, p 410]. Initial raytrace modelling (outside the scope of this article) using the PHaRLAP radio wave propagation toolbox [48, 49] indicates that in the cases of the Hungary and Slovenia to UK paths at 50 MHz, the downward characteristic waves will be very close to pure circular polarization. If this is the case, then if only one characteristic mode were present [29] the downward wave would also have almost circular polarization, not clearly elliptical as the study results show. Therefore, the implication of the observed elliptical polarization is that both O and X are present in the signals monitored for this study.

On the assumption that the characteristic waves are indeed circularly polarized, it can be shown that the ellipse tilt angle of the combined polarization that emerges from the ionosphere will depend only on the phase difference between O and X. The characteristic wave phase difference can, in turn, be shown to depend on the ionization gradient within the sporadic-E layer. Therefore, the magnetoionic model can, in principle, explain the variability of axial tilt as the ionization density gradient changes.

The axial ratio and sense of rotation of the combined wave, however, will depend on the amplitude relationship between the O and X waves, in which case the experimental results (see, for example, Figure 6) imply that sometimes the amplitude ratio is itself highly variable. Absorption cannot explain this variation: non-deviative absorption at 50 MHz is very low and the difference in attenuation between the two characteristic modes is negligible. Explanation of the observed polarization properties may, therefore, require consideration of other factors, such as morphological effects, or characteristic mode coupling. This will be the subject of a future article.

4.2. Application to understanding the physical properties of sporadic-E layers

Prior work on oblique propagation paths [50,51] attempted to use measured sporadic-E transmission loss, along with Es critical frequency at the reflection point, to deduce the distribution of electron density in sporadic-E layers. Necessarily, this work made a number of assumptions about the structure of Es, specifically that it is an extremely thin ionized layer.

Our approach, using polarization data to tease out information about the characteristic waves based on a magnetoionic analysis, may offer a more convincing alternative. In principle, it will be possible to establish the ionization gradient within the Es cloud and morphological/coupling models could also be tested against the experimental data. This will be the focus of further work.

5. Conclusions

This article reports the results of a polarization measurement campaign in the summer of 2018, which gathered a large amount of data at a receiving station in the south of the UK using six European 50 MHz amateur radio beacon transmitters as signal sources. Great circle paths were selected to be at a range of distances and a range of orientations to the Earth's magnetic field.

Signals reflected from intense midlatitude sporadic-E clouds were found to be overwhelmingly elliptically polarized, across multiple paths and across multiple Es events, despite the fact that they were transmitted with nominally linear polarization. Indications were also observed of the systematic variation of this behaviour with the angle of the path to the geomagnetic field at the reflection point. We have shown that neither scattering nor 'specular reflection' could produce the observed polarization behaviour, therefore the results represent, for all the examples recorded, strong evidence that signals were reflected by magnetoionic double refraction.

This technique has the potential to give further insight into the nature and structure of sporadic-E clouds. The focus of the next phase of work will be to explore the mechanisms producing the observed polarization states in more detail, and to relate that behaviour to the physical characteristics of the sporadic-E layers. This will be the subject of a further article.

Supplementary Materials: The following supporting information can be downloaded at: www.mdpi.com/xxx/s1. Video S1: Real-time replay of polarization ellipse – Slovenia (one minute). Video S2: Real-time replay of polarization ellipse – Hungary (one minute). Video S3: Real-time replay of polarization ellipse – Faroe Islands (two minutes).

Author Contributions: Conceptualization, C.D., C.M., B.W.; methodology, C.D.; software, C.D., B.W.; validation, C.D., C.M.; formal analysis, C.D.; investigation, C.D.; resources, C.D.; data curation, C.D.; writing—original draft preparation, C.D.; writing—review and editing, C.D., C.M., R.W, B.W.; visualization, C.D.; supervision, C.M., R.W.; project administration, C.D., C.M.; funding acquisition, C.M. All authors have read and agreed to the published version of the manuscript.

Funding: This research was funded by the University of Bath, which sponsored C.D.'s PhD research, and the UK Natural Environment Research Council via C.M.'s KE Fellowship, NE/P006450/1. The APC was funded by the UK Natural Environment Research Council, NE/P006450/1. B.W. is funded by INFRAIA-02-2020, ID 101007599, as part of the project "Plasmasphere Ionosphere Thermosphere Integrated Research Environment and Access services: A Network of Research Facilities (PITHIA-NRF)," https://www.pithia-nrf.eu/.

Institutional Review Board Statement: Not applicable.

Informed Consent Statement: Not applicable.

Data Availability Statement: (link TBC).

Acknowledgments: The authors would like to acknowledge the work of the builders and operators of the amateur radio beacons monitored for this study.

Conflicts of Interest: The authors declare no conflict of interest.

References

1. Smith, E. K.; Igarashi, K. VHF sporadic E – a significant factor for EMI. In *Proc. Int. Symp. EMC* **1997**, 29-32. doi: 10.1109/ELMAGC.1997.617067
2. Yue, X.; Schreiner, W. S.; Pedatella, N. M.; Kuo, Y. H. Characterizing GPS radio occultation loss of lock due to ionospheric weather. *Space Weather* **2016**, 14(4), 285-299. doi: 10.1002/2015SW001340
3. Whitehead, J. D. Recent work on mid-latitude and equatorial sporadic-E. *Journal of atmospheric and terrestrial physics* **1989**, 51(5), 401-424. doi: 10.1016/0021-9169(89)90122-0
4. Mathews, J. D. Sporadic E: current views and recent progress. *Journal of atmospheric and solar-terrestrial physics* **1998**, 60(4), 413-435. doi: 10.1016/S1364-6826(97)00043-6

5. Haldoupis, C. A tutorial review on sporadic E layers. In Abdu, M., Pancheva, D. (eds) *Aeronomy of the Earth's Atmosphere and Ionosphere*, IAGA Special Sopron Book Series, vol 2. Springer, Dordrecht; 2011; pp. 381-394. doi: 10.1007/978-94-007-0326-1_29
6. Smith, E. K. Temperate zone sporadic-E maps (foEs > 7 MHz). *Radio Science* **1978**, 13(3), 571-575. doi: 10.1029/RS013i003p00571
7. Smith, E. K. *Worldwide Occurrence of Sporadic E* (Vol. 582). US Department of Commerce, National Bureau of Standards, 1957; pp. 178-183. doi: n/a
8. Smith, L. G.; Mechtly, E. A. Rocket observations of sporadic-E layers. *Radio Science* **1972**, 7(3), 367-376. doi: 10.1029/RS007i003p00367
9. Christakis, N.; Haldoupis, C.; Zhou, Q.; Meek, C. Seasonal variability and descent of mid-latitude sporadic E layers at Arecibo. In *Annales Geophysicae* **2009**, 27, 3, 923-931. doi: 10.5194/angeo-27-923-2009
10. Grebowsky, J. M.; Bilitza, D. Sounding rocket data base of E-and D-region ion composition. *Advances in Space Research* **2000**, 25(1), 183-192. doi: 10.1016/S0273-1177(99)00916-3
11. From, W. R.; Whitehead, J. D. On the peculiar shape of sporadic-E clouds. *Journal of Atmospheric and Terrestrial Physics* **1978**, 40(9), 1025-1028. doi: 10.1016/0021-9169(78)90006-5
12. Kopp, E. On the abundance of metal ions in the lower ionosphere. *Journal of Geophysical Research: Space Physics* **1997**, 102(A5), 9667-9674. doi: 10.1029/97JA00384
13. Mathews, J. D.; Zhou, Q.; Philbrick, C. R.; Morton, Y. T.; Gardner C. S. Observations of ion and sodium layer coupled processes during AIDA. *J. Atmos. Terr. Phys.*, 1993, 55, 487–498. doi:10.1016/0021-9169(93)90083-B
14. Yuan, T.; Wang, J.; Cai, X.; Sojka, J.; Rice, D.; Oberheide, J.; Criddle, N. Investigation of the seasonal and local time variations of the high-altitude sporadic Na layer (Nas) formation and the associated midlatitude descending E layer (Es) in lower E region, *J. Geophys. Res. Space Physics* **2014**, 119, 5985– 5999. doi:10.1002/2014JA019942.
15. Cai, X.; Yuan, T.; Eccles, J. V.; Raizada, S. Investigation on the distinct nocturnal secondary sodium layer behavior above 95 km in winter and summer over Logan, UT (41.7°N, 112°W) and Arecibo Observatory, PR (18.3°N, 67°W). *Journal of Geophysical Research: Space Physics* **2019**, 124, 9610– 9625. doi:10.1029/2019JA026746
16. Whitehead, J. D. The formation of the sporadic-E layer in the temperate zones. *Journal of Atmospheric and Terrestrial Physics* **1961**, 20(1), 49-58. doi: 10.1016/0021-9169(61)90097-6
17. Haldoupis, C.; Pancheva, D.; Singer, W.; Meek, C.; MacDougall, J. An explanation for the seasonal dependence of midlatitude sporadic E layers. *Journal of Geophysical Research: Space Physics* **2007**, *112*(A6). doi: 10.1029/2007JA012322
18. Qiu, L.; Zuo, X.; Yu, T.; Sun, Y.; Qi, Y. Comparison of global morphologies of vertical ion convergence and sporadic E occurrence rate. *Advances in Space Research* **2019**, 63(11), 3606-3611. doi: 10.1016/j.asr.2019.02.024
19. Yamazaki, Y.; Arras, C.; Andoh, S.; Miyoshi, Y.; Shinagawa, H.; Harding, B. J. et al. Examining the wind shear theory of sporadic E with ICON/MIGHTI winds and COSMIC-2 Radio 2 occultation data. *Geophysical Research Letters* **2022**, 49, e2021GL096202. doi: 10.1029/2021GL096202
20. Sobhkhiz-Miandehi, S.; Yamazaki, Y.; Arras, C.; Miyoshi, Y.; Shinagawa, H. Comparison of the tidal signatures in sporadic E and vertical ion convergence rate, using FORMOSAT-3/COSMIC radio occultation observations and GAIA model. *Earth, Planets and Space* **2022**, *74*(1), 1-13. doi: 10.1186/s40623-022-01637-y
21. Deacon, C. J.; Witvliet, B. A.; Steendam, S. N.; Mitchell, C. N. Rapid and accurate measurement of polarization and fading of weak VHF signals obliquely reflected from sporadic-E Layers. *IEEE Transactions on Antennas and Propagation* **2020**, *69*(7), 4033-4048. doi: 10.1109/TAP.2020.3044654
22. Chartier, A. T.; Hanley, T. R.; Emmons, D. J. Long Distance Propagation of 162-MHz Shipping Information Links Associated with Sporadic-E, *Atmos. Meas. Tech. Discuss* **2022**, doi: 10.5194/amt-2022-214, preprint in review
23. Miya, K.; Shimizu, K.; Kojima, T. Oblique-incidence sporadic-E propagation and its ionospheric attenuation *Radio Sci*. **1978**, *13*, 559-570. doi: 10.1029/rs013i003p00559
24. Harvey, J.A. Movement of sporadic E ionization, *Austr. J. Phys.* **1955**, *8*, 523-534. doi: 10.1071/ph550523
25. Tau, K. A. Theoretical Study of Sporadic-E Structure in the Light of Radio Measurements. In *Ionospheric Sporadic E*; Smith, E.K.; Matsushita, S, Eds., International Series of Monographs on Electromagnetic Waves, Pergamon, **1962**, pp. 235-257. doi: 10.1016/b978-0-08-009744-2.50024-2
26. Rawer, K. Definitions of frequency parameters of Es–layers and their accuracy. In *Ionospheric Sporadic E*, Smith, E.K.; Matsushita, S, Eds., International Series of Monographs on Electromagnetic Waves, Pergamon, **1962**, pp. 151-165. doi: 10.1016/b978-0-08-009744-2.50017-5
27. Appleton, E.V.; Builder, G. The ionosphere as a doubly-refracting medium. *Proc. Phys. Soc. (1926-1948)* **1933**, *45*(2), 208-220. doi: 10.1088/0959-5309/45/2/307
28. Ratcliffe, J.A. *The magneto-ionic theory and its applications to the ionosphere*, Cambridge University Press, **1959**. doi: 10.1002/qj.49708536525
29. Witvliet B.A.; van Maanen, E.; Petersen, G.J.; Westenberg, A.J.; Bentum, M.J.; Slump, C.H.; Schiphorst, R. Measuring the isolation of the circularly polarized characteristic waves in NVIS propagation [Measurements Corner], *IEEE Antennas Propag. Mag.* **2015** *57*(3), 120–145. doi: 10.1109/map.2015.2445633

30. EBU Technical Centre, "Ionospheric propagation in Europe in VHF television band I," EBU Technical Document TECH 3214, Vol. I and II, European Broadcasting Union, Brussels, Belgium **1976**. doi: not available
31. Edwards, K. J.; Kersley, L.; Shrubsole, L. F. Sporadic-E propagation at frequencies around 70 MHz, *Radio Electron. Eng.***1984**, *54* (5), 231–237. doi: 10.1049/ree.1984.0057
32. Ichinose, M.; Kainuma, S. Polarization characteristics of VHF radio waves reflected by the Es-layer, *IEEE Trans. Broadcast* **1996**, *42*, 82-87. doi: 10.1109/11.506823
33. IEEE Std 145-2013, IEEE Standard for Definitions of Terms for Antennas, **2014**. doi: 10.1109/ieeestd.2014.6758443
34. IEEE Std 149-1979, IEEE Standard Test Procedures for Antennas, **1979**. doi: 10.1109/ieeestd.1979.120310
35. Mott, H. *Polarization in antennas and radar*, Wiley, New York, **1986**. doi not available
36. Stutzman, W.L. *Polarization in electromagnetic systems*, Artech, **2018**. doi not available
37. Poincaré, H. *Théorie mathématique de la lumière II.: Nouvelles études sur la diffraction.--Théorie de la dispersion de Helmholtz. Leçons professées pendant le premier semestre 1891-1892* (Vol. 1). G. Carré. **1889.** doi not available
38. Deschamps, G.A. Geometrical representation of the polarization of a plane electromagnetic wave. *Proc. Ire*, **1951**, *39*(5), 540-544. doi: 10.1109/jrproc.1951.233136
39. Deschamps, G.; Mast, P. Poincaré sphere representation of partially polarized fields. *IEEE Transactions on Antennas and Propagation* **1973**, *21*(4), 474-478. doi: 10.1109/tap.1973.1140516
40. Arras, C.; Wickert, J.; Beyerle, G.; Heise, S.; Schmidt, T.; Jacobi, C. A global climatology of ionospheric irregularities derived from GPS radio occultation. *Geophysical research letters* **2008**, 35(14). doi: 10.1029/2008GL034158
41. Baggaley, W.J. Seasonal characteristics of daytime Es occurrence in the Southern Hemisphere, *J. Atmos. Terr. Phys* **1985**, 47 (6), 611-614. doi: 10.1016/0021-9169(85)90044-3
42. Deacon, C.; Mitchell, C.; Watson, R. Consolidated Amateur Radio Signal Reports as Indicators of Intense Sporadic E Layers. *Atmosphere*, **2022**, 13, 906. doi:10.3390/atmos13060906
43. Chulliat, A.; Macmillan, S.; Alken, P.; Beggan, C,; Nair, M.; Hamilton, B.; Woods, A.; Ridley, V.; Maus, S.; Thomson, A. *The US/UK World Magnetic Model for 2015-2020: Technical Report*, National Geophysical Data Center, NOAA, 2015. doi: 10.7289/V5TB14V7
44. Davies, K. *Ionospheric Radio*, Peter Peregrinus, London, **1990**. doi: 10.1049/pbew031e
45. Bailey, D.K.; Bateman, R.; Kirby, R.C. Radio transmission at VHF by scattering and other processes in the lower ionosphere. *Proceedings of the IRE* **1955**, 43(10), 1181-1230. doi: 10.1109/jrproc.1955.277933
46. Hecht, E. *Optics 2nd edition*, Addison-Wesley, Reading, MA, **1987.** doi not available
47. Born, M.; Wolf, E. *Principles of optics. sixth (corrected) edition*, Cambridge University Press, **1997.** doi not available
48. Cervera, M. A.; Harris, T.J. Modeling ionospheric disturbance features in quasi-vertically incident ionograms using 3-D magnetoionic ray tracing and atmospheric gravity waves, *J. Geophys. Res. Space Physics*, **2014,** *119*, 431–440, doi:10.1002/2013JA019247.
49. PHaRLAP is available from https://www.dst.defence.gov.au/our-technologies/pharlap-provision-high-frequency-raytracing-laboratory-propagation-studies (accessed on 29 October 2022).
50. Tau, K. The Structure of the Sporadic E Layer Detected from VHF Ionospheric Propagation, *Radio Science*, **1966**, *1*(2), 132-144. doi: 10.1002/rds196612132
51. Bramley, E.N. Very-high-frequency wave propagation by the temperate-latitude sporadic-E layer, *J. Atmos. Terr. Phys*, **1972**, *34*(9), 1495-1505. doi: 10.1016/0021-9169(72)90081-5